PARALLELIZING CPAIMD USING CHARM++

BY

RAMKUMAR VENKAT VADALI

B.Tech., Indian Institute of Technology, Madras, 2001

THESIS

Submitted in partial fulfillment of the requirements
for the degree of Master of Science in Computer Science
in the Graduate College of the
University of Illinois at Urbana-Champaign, 2003

Urbana, Illinois

Abstract

Many important problems in material science, chemistry, solid-state physics, and biophysics require a modeling approach based on fundamental quantum mechanical principles. A particular approach that has proved to be relatively efficient and useful is *Car-Parrinello ab initio molecular dynamics* (CPAIMD). Parallelization of this approach beyond a few hundred processors is challenging, due to the complex dependencies among various subcomputations, which lead to complex communication optimization and load balancing problems. This thesis presents a scalable parallelization of CPAIMD using Charm++. The computation is modeled using a large number of virtual processors, which are mapped flexibly to available processors with assistance from the Charm++ runtime system. Charm++ allows the use of "parallel" libraries to facilitate common operations such as parallel 3-D FFTs. We present results for a benchmark (based on PINY MD) with 32 water molecules (128 states) scaling to more than 1000 processors, setting a precedent for this problem.

To my parents.

Acknowledgments

I would first like to thank my adviser, Professor Laxmikant Kale, for his guidance during my work under him. He was a constant source of encouragement and insight and motivated me to strive for betterment. This work would not have been possible without him.

Thanks to my senior colleagues at the Parallel Programming Laboratory: Sameer Kumar, Gengbin Zheng and Orion Lawlor. They have provided valuable inputs to this work. Sameer and Gengbin particularly helped me a lot by helping me use their libraries and making a lot of my work easier. Thanks to Chee Wai, for being the fun person that he is. Thanks also to my colleagues in PPL, who have been great friends, and made my stay memorable.

I would like to thank my parents for their support and guidance. I have much to be thankful for, and they are responsible for most of it.

Table of Contents

List of Tables

List of Figures

Chapter 1

Introduction

Car-Parrinello *ab initio* molecular dynamics (CPAIMD) ([**?**, **?**, **?**]) can be used to study key chemical and biological processes. Moreover it is a simulation methodology that also can be employed in material science, solid-state physics and chemistry. CPAIMD methodology numerically solves Newton's equations using forces derived from electronic structure calculations performed "on the fly" as the simulation proceeds. This technique can revolutionize a host of technological problems including molecular electronics and enzyme catalysis.

Ab initio calculations have applications in nanoscience and industrial catalysis, for analyzing the ability of complex surfaces to catalyze chemical reactions and in biocatalysis, to simulate catalytic reactions in enzymes. Our code provides a framework for developing such simulation environments. A particularly relevant application involves treating most of the protein and water solvent using an empirical force field (as is done in a classical MS program such as NAMD [**?**]) while treating the substrate and active site region of the protein with a CPAIMD description (called a hybrid or QM/MM approach).

In order to exploit the power of this algorithm to the fullest, it is necessary to achieve efficient parallelization on large parallel machines available today. This is made difficult by several factors. The CPAIMD method involves multiple 3-D FFTs. Parallel 3-D FFTs are known to be communication intensive due to the all-to-all nature of the communication they require. Efficient concurrent execution of hundreds of independent 3D FFTs is a challenging issue. There are several other phases in the method that involve potentially large data movements, with relatively little computation. Parallelization of these phases necessitates complex trade-offs between memory, load balance, and communication costs. Such issues make scalability of the code a non-trivial problem to solve.

Often, current MPI-based implementations of CPAIMD suffer from limited scalability, especially if they restrict their parallelism to the number of states. Our implementation uses Charm++, which offers the benefits of virtualization, and enables us to demonstrate better scalability and per-iteration times even on small problem sizes.

In the next chapter, we describe the basic steps and data structures used by the sequential algorithm, and expose the data dependencies. We also describe our approach to parallelizing this computation, based on the idea of processor virtualization. Chapter 3 describes a parallel library that can be used to perform transpose-based 3-D FFTs. Chapter 4 describes various optimizations we developed while scaling the implementation to over thousand processors. The optimizations are illustrated with a series of intermediate performance snapshots. Chapter 5 presents some concluding remarks about the lessons learned and future research.

Chapter 2

The Computation

In a Car-Parrinello (CP) simulation, the electron density of the ground electronic state is calculated using density functional theory (DFT), and is used to compute the forces acting on the ions. The algorithm is summarized in its essential parts in the flowchart in figure 2.1. An overview of the data structure and dependencies of the CPAIMD algorithm is shown in figure 2.2. We now describe the algorithm from the point of view of parallelization.

Figure 2.1: Schematic flowchart of our implementation of the CP algorithm

The basic objects are n_s electronic orbitals (or states), each of which is represented as a set of fourier coefficients in a 3-dimensional "g-space" (or reciprocal space). These coefficients are read in directly from files generated from a simulation. There is a file corresponding to each state and is named "state$i$.out", where i ranges between 1 and n_s. In "real-space", each state is represented by a 3-D array ($N \times N \times N$) of complex numbers. The g-space representation should, in principle, be a dense $N \times N \times N$ array. However, an energy cutoff is employed, which leads to only a fraction of the cube being non-zero: a sphere of radius proportional to $N/4$ comprises the non-zeroes. The aggregated density function ρ is represented by another single 3D array of dimension N. Again, its reciprocal-space representation is also necessary.

In figure 2.3, the decomposition of orbitals and densities is shown along with the progress

Figure 2.2: A serial view of the CPAIMD algorithm, showing data dependences

of the algorithm. The algorithm begins with the g-space representations of each state. Given n_s states, the algorithm first converts each state to "real-space" using 3-D FFTs (phase I). The real-space representation of all states are squared and summed to obtain the electronic density ("reduction" operations in phase II). The fourier coefficients of the density are obtained using an inverse 3-D FFT. Now two independent computations are to be performed with the density and the fourier coefficients of the density. The "exchange and correlation energy" requires the density in real space (phase III), and the "Hartree energy" requires the fourier coefficients of the density (IV) (and the atomic structure factor, which can be computed using particle-mesh methods). The derivative of sum of the these energies, along with the states, is used to compute forces via multiple 3-D inverse FFTs (multicast in phase V and inverse FFTs in phase VI).

The fourier coefficients of the orbitals are also used to compute the "non-local" energy and forces using matrix reductions (phase IX). The forces computed from the electronic density and the non-local computation are summed and subjected upon the orbitals. Finally it is necessary to orthonormalize the orbitals, which requires a set of matrix multiplications and transposes (phases VII and VIII).

2.1 Parallelization

We parallelized this application using the *processor virtualization* approach [**?**], supported by the Charm++ ([**?**]) parallel programming system. In this approach, the work is divided into a large number of objects or virtual processors (VPs); the computation is initially expressed in terms of these virtual processors, ignoring the issue of which physical processors they are mapped to. Then, either the runtime system or users can optimize their program by separately specifying or changing the mapping – either initially or even during the execution of program. In Charm++, the VPs are C++ objects (called *chares*), which communicate with each other via asynchronous method invocations (also called messages). [1] Essentially, Charm++ allows programmers to separate the issue of decomposition and mapping.

Figure 2.3: Parallel structure of our implementation. Roman numbers indicate phases

2.1.1 Decomposition of Data

In our implementation, the orbitals in g-space and real-space are each decomposed into planes in a grid. The work related to each plane is performed by a Charm++ virtual processor (or chare). In accordance with our philosophy of processor virtualization, the number of virtual processors depends only on issues such as overhead, but is independent of the total number of physical processors. A collection G holds *objects* $G(s, p)$ corresponding to p'th plane of the s'th state in g-space. The plane index p is identical to the x co-ordinate in g-space, gx, and the object $G(s, gx)$ houses the coefficients $\Psi(s, gx, gy, gz)$ for all values of gy and gz. Similarly, another collection R holds real-space planes $R(s, p)$ corresponding to the p'th plane of s'th state, again. However, the axis of decomposition is different for G and R, due to the way the FFTs are implemented. The planes of G are $y - z$ planes and the planes of R are $x - z$ planes.

In addition, there are 1-dimensional chare arrays for representing the charge density, ρ in real and g-space. The 1-D chare array for the real-space density is represented by "rhoRealProxy", and that for the g-space density is represented by "rhoGProxy".

The non-local computation (phase IX) needs information on the particle positions and charges. Moreover, the g-space data is also needed, and since this data is already present in G, we create another chare array (represented by "particlePlaneProxy"), which uses the data from G. This is described in more detail in section 2.1.4.

For concreteness, it is worth noting that with $n_s = 128$ states, and N=100, this scheme

[1]The Charm runtime system (RTS) supports multiple types of virtual processors. In *Adaptive MPI* [?], for example, each virtual processor is a user-level thread implementing an MPI "process". C++ objects are just one type of a virtual processor

decomposes the computation into 12,800 virtual processors for representing states in real-space, and about half as many virtual processors representing the non-empty planes of g-space. In addition, there are 100 virtual processors each for representing density in real-space and reciprocal space.

The resultant decomposition of the problem is shown in equation 2.3. We next describe specific parallel implementation choices and optimization issues. The mapping scheme used for assigning virtual processors to physical processors is described in figure 2.1.2. However, to understand the motivations behind the mapping used, we must first describe how the Orthonormalization was parallelized.

2.1.2 Orthonormalization

This part of the computation (i.e. phases VII and VIII) is performed after the modification of the states in g-space. We have adopted the Lówdin method for orthonormalization. We perform the matrix computations involved in parallel, but do the matrix transformation serially. This was a choice made on the basis of the amount of time (less than 35ms) the computation takes for our problem size [2].

The matrix computation problem is that of computing a square matrix S of size n_s [3] defined as:

$$S(s,s') = \sum_{gx}\sum_{gy}\sum_{gz} \Psi(s,gx,gy,gz)\Psi^*(s',gx,gy,gz), \tag{2.1}$$

where Ψ is the plane wave function defined over state numbers s and the position vector in g-space (gx,gy,gz), housed in the collection G. Once S is computed, its inverse square root T is computed using a serial implementation of the Lówdin method that runs in time $O(n_s^3)$.

[2]The cost of the step is $O(n_s^3)$, and so for larger problem sizes, this step will have to be parallelized

[3]In our formulation, the real-space orbitals are taken to be real functions. Hence $\Psi(s,gx,gy,gz) = \Psi^*(s,-gx,-gy,-gz)$, which leads to S being symmetric and real

Using T, the orbital fourier coefficients are re-computed as:

$$\Psi(s, gx, gy, gz) = \sum_{s'} T(s, s')\Psi(s', gx, gy, gz) \tag{2.2}$$

Let us consider the parallel implementation of equations 2.1 and 2.2. Figure 2.5 shows a pseudo-code version of the computation that has to be parallelized. $S(s, s')$ is computed in two steps, taking advantage of the fact that the states in g-space are decomposed into multiple planes for each state. Since the plane $G(s, gx)$ houses all coefficients $\Psi(s, gx, gy, gz)$, the computation of $S(s, s')$ is split into two parts - computing an intermediate value $S_{aux}(s, s', gx)$ and using that to compute $S(s, s')$.

$$S_{aux}(s, s', gx) = \sum_{gy} \sum_{gz} \Psi(s, gx, gy, gz)\Psi^*(s', gx, gy, gz) \tag{2.3}$$

$$S(s, s') = \sum_{gx} S_{aux}(s, s', gx) \tag{2.4}$$

```
// initialize
foreach(s)
  foreach(s’ >= s)
    S(s, s’) = 0.0

// S-computation
foreach(s)
  foreach(s’ >= s)
    foreach(gx)
      foreach(gy)
        foreach(gz)
          S(s,s’) += psi[s,gx](gy,gz) * psi[s’,gx]](gy,gz).conjugate()
```

Figure 2.4: The process involved in S-matrix computations

Equation 2.3 shows that all coefficients of $G(s, gx)$ and $G(s', gx)$ need to “meet”. A ring-based approach seems to be the natural choice to implement this. This approach involves n_s steps. In the first step, each $G(s, gx)$ sends all its g-space data to $G((s + 1)\%n_s, gx)$, upon

```
// initialize
foreach(s)
  foreach(gx)
    foreach(gy)
      foreach(gz)
        new_psi[s,gx](gy,gz] = 0.0

// T-computation, i.e. new psi values
foreach(s)
  foreach(s')
    foreach(gx)
      foreach(gy)
        foreach(gz)
          psi_new[s,gx] += T(s,s') * psi[s,gx](gy,gz)

foreach(s)
  copy(psi, psi_new)
```

Figure 2.5: The process involved in recomputing the g-space values using the T matrix

receipt of which, $G((s+1)\%n_s, gx)$ computes $S_{aux}(s, (s+1)\%n_s, gx)$. In each subsequent step, $G(s, gx)$ forwards the data that it received in the preceding step. This can be visualized as N rings of size n_s being formed. After n_s steps, all entries of S_{aux} would have been computed, albeit by different $G(s, gx)$. The different parts are collected in one place, using a reduction, and summed to compute the matrix S, as per equation 2.4. Once T is computed, relevant portions are communicated to all $G(s, p)$. A method similar to that described above is used to calculate the new values of the orbital coefficients as defined in equation 2.2. However, each hop in the ring results in the new values of Ψ, rather than S_{aux}.

This method is clearly better than the naive method of direct all-to-all communication between all $G(s, p)$, because during each step of the ring, only n_s messages are in transit, reducing network congestion. But the problem is that the data of each $G(s, p)$ is still sent n_s times. Since the amount of g-space data is more than 100MB, this would imply tremendous communication costs. Also, the size of the rings formed is n_s, which implies a long delay before the S matrix is computed.

To alleviate these problems, we used an alternative approach (we call it a **block-pairs** approach, following a standard technique for all-pairs computation) where the data of $G(s, gx)$ and $G(s', gx)$ "meets" at a virtual processor devoted to computing $S_{aux}(s, s', gx)$. We create a collection S_{arr}, each element of which is responsible for computing a $\gamma \times \gamma$ region of the S_{aux} matrix, where γ is a configurable constant.

Figure 2.6: Computing the entries of the S matrix: each array element $S_{aux}(s, s'), s \leq s'$ computes at least γ entries of the S matrix.

$S_{arr}(\frac{s}{\gamma}, \frac{s'}{\gamma}, gx)$ receives g-space data from $G(s, gx) \ldots G(s+\gamma-1, gx)$ and $G(s', gx) \ldots G(s'+\gamma-1, gx)$, i.e., 2γ messages. Using this data, a $\gamma \times \gamma$ part of the S_{aux} matrix can be computed as per equation 2.3. Also, as S is symmetric, $S_{arr}(\frac{s}{\gamma}, \frac{s'}{\gamma}, gx)$ can do the work of $S_{arr}(\frac{s'}{\gamma}, \frac{s}{\gamma}, gx)$. So, only those $S_{arr}(s, s', gx)$ are created, for which $s \geq s'$. This is illustrated in fig 2.6. Once the S_{aux} elements are ready, S can be calculated by performing a reduction operation over S_{arr}.

Since the original g-space data is present in the S_{arr} array, the new g-space data can be computed using its elements. To compute the new state values as per equation 2.2, each $S_{arr}(\frac{s}{\gamma}, \frac{s'}{\gamma}, gx)$ needs a $\gamma \times \gamma$ portion of the T matrix. Once this is made available using a multicast operation [4] , it can compute new g-space values for the $G(s, gx) \ldots G((s+\gamma-1), gx)$ and $G(s, gx) \ldots G((s+\gamma-1), gx)$ and communicate the new values to them.

To compute the communication cost here, we have to consider it from the point of view of each g-space plane. Each $G(s, gx)$ has to multicast its data to $\frac{n_s}{\gamma}$ S_{arr} elements. Hence the total g-space data is communicated $\frac{n_s}{\gamma}$ times, instead of n_s times, as in the case of the ring method. The larger γ is, the lesser the communication cost is. Also, note that, the higher γ is, the greater is the data reuse. If γ is n_s, then each set of g-space data has to be sent only once. But we had to choose $\gamma \leq 32$ to prevent the computation cost per S_{arr} element from becoming too high.

But the non-local communication on larger number of processors still turned out to be

[4]We found that communicating the entire T matrix to all processors using a machine level broadcast was more efficient than multicasts of small $\gamma \times \gamma$ portions of the T matrix

pretty high when $\gamma \leq 32$ was used. To keep data reuse high while keeping the parallelization at reasonable levels, we utilized one more dimension of parallelism - division of g-space data in the planes. In other words, the computation of each $S_{aux}(s, s', gx)$ can further be parallelized over the points of data in the g-space plane $G(s, gx)$.

$$S_{aux}(s, s', gx) = \sum_{chunk\ of\ g-space\ c=0}^{\mathcal{C}} S_{aux}(s, s', gx, c) \tag{2.5}$$

$$S_{aux}(s, s', gx, c) = \sum_{gy\ in\ c} \sum_{gz\ in\ c} \Psi(s, gx, gy, gz)\Psi^*(s', gx, gy, gz) \tag{2.6}$$

In the implementation, this causes the collection S_{arr} to become indexible by 4 indices. Each $S_{arr}(s, s', gx, c)$ computes $S_{aux}(s, s', gx, c)$. Importantly, now γ can be set to n_s but the amount of parallelism can be increased by dividing the g-space data in each plane to more than one chunk.

At the time of writing this document, this dimension of parallelism was not explored, and the rest of the document will deal with the case where the number of chunks is 1, so the 4-dimensional collection S_{arr} reduces to a 3-dimensional array.

Mapping

The Charm++ system has a default mapping (of virtual processors to real processors) for chare arrays. The Charm++ RTS is also capable of automatically changing the mapping to achieve load balance. However, here, the load for each virtual processor is predictable and static (i.e. doesn't change during the run). There are also opportunities for intelligent mapping to simultaneously optimize load balance and communication overhead. So, we decided to define the mapping manually at the application level.

The mapping of the real-space objects is influenced by the multicast (fig 2.3, phase V) from density objects to real-space objects. It is desirable to have as many multicast target objects on the same processor as possible. The targets in this case are the planes in real-space, coming from different states but the same spatial region. This leads to a mapping

Figure 2.7: CPAIMD-specific 3-D FFT implementation. 1-D FFTs in the "j" direction are performed first in the planes. Pencils of data are communicated and two sets of 1-D FFTs are done in the "i-k" planes.

function

$$pe(R(s,p)) = \mathcal{P} \times \frac{p \times n_s + s}{N \times n_s} \tag{2.7}$$

where $\mathcal{P}$ is the total number of processors Note that we could also have tried to minimize communication during the concurrent transposes with g-space planes (phases I and VI) by assigning multiple real-space planes with same state index but different plane index together. But the amount of communication involved in the transpose phase is smaller owing to the sparseness of data in g-space.

The mapping of the g-space objects is slightly more complicated. In section 2.1.2, we saw that $S_{aux}(\frac{s}{\gamma}, \frac{s'}{\gamma}, p)$ requires communication with $G(s \ldots (s+\gamma-1), p)$ and $G(s' \ldots (s'+\gamma-1), p)$. Hence this part of the computation would benefit if $G(*, p)$ were co-located, as is the case with R. But using a mapping similar to that in equation 2.7 causes a problem of load-imbalance: the distribution of load among planes in g-space follows the distribution of points among discrete planar sections of a sphere. We describe how we dealt with this load imbalance problem using different mapping schemes in section 4.

3D FFTs

Parallel 3-D FFTs have been dealt with by Cramer et. al., who use a transpose-based method ([?]) and Haynes et. al., who use an alternative method with $\log(n)$ stages ([?]). The multi-stage method has the advantage of lower per-message(α) cost but suffers from higher per-byte(β) cost. We chose the transpose method to parallelize the FFTs since we can control the number of messages exchanged through the libraries provided in Charm++, and reduce the α cost. The 1-D and 2-D (serial) FFTs were performed by using FFTW [?]. The transpose method requires the FFT to be performed in stages, first 2-D then 1-D or vice-versa. We chose to do the 1-D FFTs and then 2-D FFTs as the orbitals have a sparse distribution in their 3-D grid (fig 2.7(a)), in a sphere. Due to our choice, we could control the number of FFT operations at a finer grainsize. Also, the transpose becomes less communication intensive since the amount of non-zero data to be sent is reduced. This is illustrated in figure 2.7

2.1.3 Performing the Multiple Parallel 3-D FFTs

The algorithm requires multiple (n_s) 3-D FFTs to be performed. We perform these *concurrently* using Charm++. In each 3-D FFT, there is computation (FFT) part and a communication (transpose) part. On each processor, planes belonging to different states can reside, and these are involved in independent 3-D FFTs. We are able to overlap the computation of one 3-D FFT with the communication of several other 3-D FFTs, as seen in figure 2.8. This is especially relevant on machines such as PSC Lemieux, where the nodes have a communication co-processor that allows the main processor to continue computation while it transfers data via remote DMA without processor intervention (as seen in [**?**]). This overlap of computation and communication is made possible by Charm++, and its advantage over the MPI-like synchronous model can not be overemphasized.

2.1.4 Non-local Computation

This computation (phase IX) involves computing the non-local matrix and using it to compute forces. The non-local matrix “Z” is a $n_s \times N \times N \times N \times n_{atom}$ matrix. The non-local component of the forces requires both particle data (responsible for the n_{atom} part) and g-space data (responsible for the $N \times N \times N$ part).

The particle data is replicated on all processors using a Charm++ group. The g-space data is decomposed using the G array and to access it, the objects performing the non-local computation have to “borrow” it. This is achieved by creating a collection A that is bound

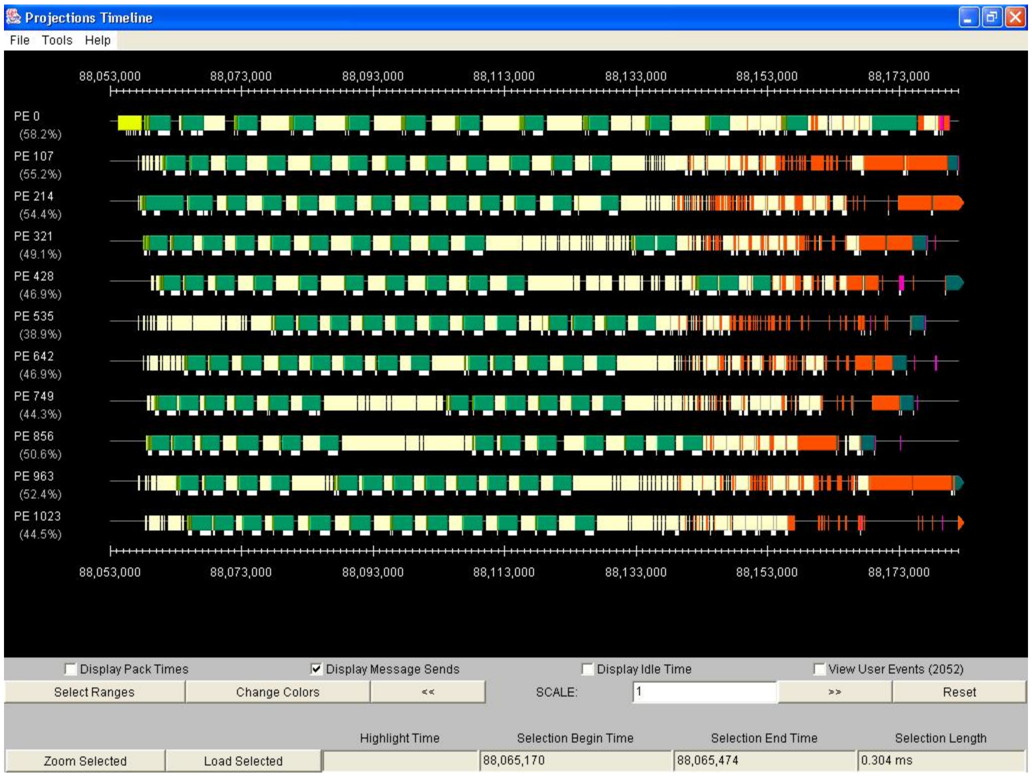

SCALE: 1

Selection Begin Time: 88,065,170

Selection End Time: 88,065,474

Selection Length: 0.304 ms

Figure 2.8: Overlapped Transposes in concurrent FFTs in Phase I, as seen in a *timeline* view. The x axis shows the time, and the y axis shows messages being processed on a subset of the processors. Some messages (show with tails) create new messages, the communication of which is overlapped with processing of other messages

Figure 2.9: Subroutines used in the particle computation

to the collection G. A has exactly one object for each object in G, and $A(s,p)$ is always present on the same processor as $G(s,p)$.

To access the g-space data, $A(s,p)$ performs a local computation to gain access to the object $G(s,p)$, and copies the g-space data. This allows it to compute a part of the Z matrix (using the subroutine "computeZ(...)", as seen in figure 2.9, corresponding to its state index s, x-index p and all values of y-index, z-index and atom-index. Thus the Z matrix is computed in a distributed manner.

Next the Z matrix is reduced over g-space. To do this, $A(s,p)$ first reduces it over the y and z dimensions, and objects $A(s,*)$ collectively reduce it over the x dimension. The result of the reduction is collected at $A(s,0)$ (again, refer figure 2.9). This is a essentially a vector of size n_{atom}. One such vector is present at each $A(s,0)$, and hence the reduced Z matrix is available in the form of reduced vectors.

Each reduced vector available at $A(s,0)$ is communicated back to the objects $A(s,*)$, where it is used to compute forces for the corresponding portion of g-space. These forces are added with the forces computed using the electron density.

2.1.5 The Reduction to Form Probability Density in Real Space (Phase II)

Once the 3-D FFTs are completed, thus making the states available in real-space, the electronic densities can be computed for each state. This is

$$\rho(x,y,z) = \sum_s |\Psi^r(s,x,y,z)|^2$$

Since the states are decomposed into planes, the computation of density can be parallelized over each plane index (a total of N) in real-space. Thus there are multiple (N) reductions in progress simultaneously. These involve relatively large amounts of data each, since the real-space objects are densely populated (10,000 complex numbers, for our benchmark). Our choice of mapping reduced the communication in this phase, since all the virtual processors mapped to a physical processor tend to belong to the same plane number, allowing the runtime system to add them up locally, before participating in processor-level reduction. This was automatically achieved using Charm++'s built-in support for reductions among subsets of virtual processors belonging to a single collection.

2.1.6 Rho Computations

Next, the real-space density can directly be used to compute the "Exchange-Correlation energy". This can be done as soon as the density is computed. This is seen in figure 2.10, where each plane of the density calls the subroutine “rhoRSubroutine(...)” on its data and gets the energies. After that, the fourier coefficients of the density can be used to compute the “Hartree Energy”. For this, a copy of the densities is to be subjected to an 3-D inverse FFT (phase IV), using a transpose. Now this data is subjected to “rhoGSubroutine(...)”, as seen in 2.10.

The energies thus computed are summed (in parallel) and multicasts of degree n_s are performed from each of the N planes of real-space density, to states in real-space. After performing 3-D IFFTs (phase VI) with a procedure essentially the reverse of that used for the FFTs, forces are obtained in g-space and are used to modify the states.

Figure 2.10: The serial subroutines used in the ρ computations

2.1.7 Multicasts

The multicast operations (figure 2.3, phase V) are each-to-many type of communication operations of degree n_s each. They can be performed ([?]) in several ways.

1. **Direct**: each of the N planes of ρ sends n_s messages to the corresponding real-space planes. The problem with this approach is that it deluges the network card with messages and causes inordinate delay in message delivery.

2. **K-send**: here each of N planes sends k messages, waits for a pre-specified amount of time and then sends again. This allows the network congestion to reduce and improves on the direct approach. But this method is problematic as the waiting period is difficult to guage correctly and the problem of network contention is not addressed.

3. **Ring**: In the ring method, each of the N planes sends data to one of the n_s states and then the data is forwarded to some other state. The advantage is that at any stage the number of messages in flight is P, and the network contention is reduced.

4. **Multi-Ring** The diameter of the ring determines the completion time of the multicast. To reduce the completion time, we created multiple rings of smaller diameters that performed the multicast in parallel. This approach works well with the mapping scheme described for real-space planes, where several "next-hops" in the ring reside on the same processor.

We tried each of the above methods of multicast and found that the ring method worked best. Note that the all-pairs communication involved in orthonormalization (for which the ring was not a good algorithm) is different from the communication in the multicast. In all the multicast strategies mentioned above, the total volume of communication entering a processor is identical. In contrast, the **block-pairs** approach reduces total volume of communication for the all-pairs pattern.

Chapter 3

Parallel FFT Library

The ab-initio molecular dynamics program uses parallel transpose-based 3-D FFTs in several phases (I, IV, VI). While the 3-D FFTs in phases I and VI are "sparse" (owing to the sparseness of data distribution in g-space), the 3-D FFTs in phase phase IV are "dense". This is because the data distribution in real-space is dense. Such transpose-based FFTs are a common occurrence in molecular dynamics applications ([?]), and we have developed a Charm++-based parallel library for parallel transpose-based 3-D FFTs.

The basic abstraction provided by the library is that of a set of slabs (collection of contiguous planes) belonging to 3-D space among which the 3-D FFT has to be done. As seen in figure 3, (a), the library can be used to perform or 3-D FFTs involving different data sets within the same set of objects. The user maintains the data within the slabs but all the code for the transpose and partial FFTs in provided in the library.

To use the library, some components of the usage should be understood. First, for the code to perform according to the user's desire, a configuration object has to be created. This

(a) Mul- ti- ple data- sets

```
class FFTinfo {
public:
<... constructors and accessor functions...>
        T srcProxy, destProxy; // Charm++ proxies for source and destination side

        // Plane-size specification:
        // There are srcSize[0] rows of size srcSize[1] each,
        // present in memory contiguously one after another.
        // Similarly, on the destination side, there are
        // destSize[0] rows of size destSize[1] each,
        // present in memory contiguously one after another.
        // For consistency, srcSize[1] == destSize[1]

        int srcSize[2];
        int destSize[2];

        bool isSrcSlab; // forward FFT is performed on source side
        int srcPlanesPerSlab, destPlanesPerSlab; // Slab thicknesses
        complex *dataPtr; // pointer to start of data.

};
```

Figure 3.1: Basic members of parallel FFT configuration

configuration information is captured by the class FFTinfo (figure 3.1). It contains a pointer to the data in addition to basic information such as the size of the planes, thickness of the slabs, etc.

Next comes inheritance. The library has been implemented as Charm++ *chare arrays*, which are C++ classes. To use the library, these C++ classes have to be specified as base classes. The inheritance has to be done in both the Charm++ interface description and in the C++ header file (figure 3.2). In the .ci file, the classes SrcArray and DestArray are indicated as derivatives of the library class. The code in the C++ part needs some explanation.

In this example, the FFTinfo is passed to the constructor. The FFTinfo setup is simple and is omitted. Since there are multiple data-sets that the user may wish to operate upon, the library has to maintain one instance of FFTinfo for each such data-set. The user has to setup the FFTinfos in the base class as shown in the example. In the library, the maximum number of data-sets allowed is a constant configurable at compile-time.

The easiest part is the actual usage - to perform a 3-D FFT from data-set 0 on the source to data-set 1 on the destination side, the function doFFT(0,1) needs to be called. Once the FFT and transpose is complete, the function “doneFFT(int id)” is called locally in the destination slabs. Similarly, on completion of the inverse FFTs, the function “doneIFFT(int id)” is called locally in the source slabs. The user should override the default definitions of these functions as seen in the example.

```
In Charm++ .ci file:

mainmodule app {
        extern module fftlib;
        array [1D] SrcArray: NormalSlabArray {
                entry SrcArray(NormalFFTinfo &conf);
        };

        array [1D] DestArray: NormalSlabArray {
                entry DestArray(NormalFFTinfo &conf);
        };
};

C++ inheritance:

class SrcArray: public NormalSlabArray {
 public:
  SrcArray(CkMigrateMessage *m) {}
  SrcArray(NormalFFTinfo &info):NormalSlabArray() {
                // normal setup
        plane1 = new complex[info.srcSize[0] * info.srcSize[1] * info.srcPlanesPerSlab]
        plane2 = new complex[info.srcSize[0] * info.srcSize[1] * info.srcPlanesPerSlab]

                // Library-specific code
        fftinfos[0] = new NormalFFTinfo(info);
        fftinfos[0]->dataPtr = plane1;
        fftinfos[1] = new NormalFFTinfo(info);
        fftinfos[1]->dataPtr = plane2;
  }

  void doIt(int id) {doFFT(id, id);}
  void doneIFFT(int id) {ckout << id << " Back" << endl;}
 private:
  complex *plane1, *plane2;
};
```

Figure 3.2: Example usage of the library: inheritance

Chapter 4

Performance and Optimizations

We ran our code on PSC Lemieux, a 750 node, 3000 processor cluster. Each node in Lemieux is a Quad 1Ghz Alpha server connected by Quadrics Elan, a high speed interconnect with $4.5\mu s$ latency. The runs were performed with a g-space data set representing 32 water molecules with a grid size of $100 \times 100 \times 100$.

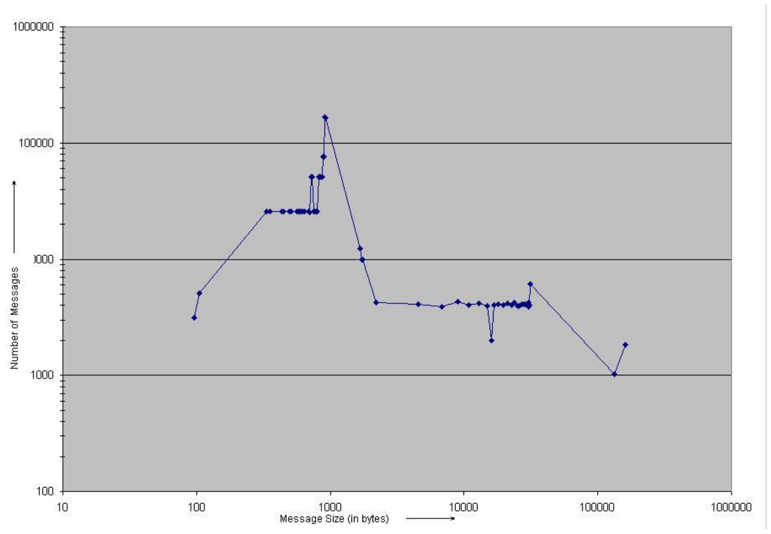

Figure 4.1: Number of non-local messages for different message sizes, on 1024 processors. There is total of 3.5 GB non-local communication per iteration.

Table 4.1 shows the scalability of the code. We achieved a peak floating point operations rate of 121 GFlops on 1536 processors. Although this is a small fraction of the machine's capability, it is acceptable due to the communication intensive nature of this application.

Figure 4.1 shows the communication behavior of our code on 1024 processors. There is a

Nodes	Processors	Time(sec)	GFLOPS	Nodes	Processors	Time(sec)	GFLOPS
8	16	13.260	4	43	129	2.2	22
16	32	6.17	8	83	258	1.3	37
32	64	3.110	15	171	513	0.680	71
64	128	2.07	23	256	768	0.600	80
128	256	1.18	41	512	1536	0.398	121
256	512	0.650	74				
512	1024	0.480	100				

Table 4.1: Execution times on PSC Lemieux, for 128 states. Using more processors per node affects performance adversely as the bandwidth is a limited resource.

total of 3.5 GB of non-local communication, with the maximum data received *per processor* being 5 MB. There are two modes of the distribution: the messages caused due to the 3-D FFTs have sizes around 1KB, and the messages involved in the matrix computations in orthonormalization have sizes around 20KB. These constitute the largest fraction of the non-local communication. Notice that there are only one or two non-local messages *per processor* that have a size greater than 100KB (multicast messages in phase V). This can be accredited to the mapping scheme used for real-space planes (eqn 2.7) along with the multicast strategy (multi-ring), which causes the most of the hops in the ring to be on-processor

To arrive at these results, we performed several optimizations, both algorithmic and platform-specific. We explain the load-balance related optimizations in detail, with intermediate and final results.

4.0.8 Effect of Mapping on Load Balance

The effect of different mapping schemes is shown in figure 4.2, with “overviews” created by the *Projections* performance tool, for 1024 processor runs. Each horizontal line corresponds to one processor, with the x-axis showing progress in time (white color indicates a busy processor). Using a map similar to equation 2.7 caused a load imbalance. The problem is seen clearly in figure 4.2, (a), where the middle processors are significantly underloaded compared with processor near 0 and 1023.

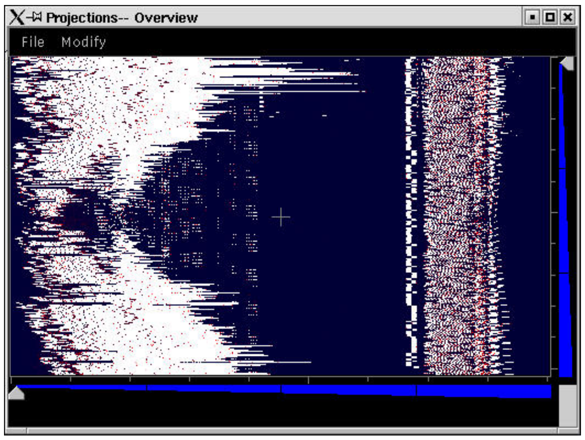

(a) Load imbalance due to phases I and IX (900ms)

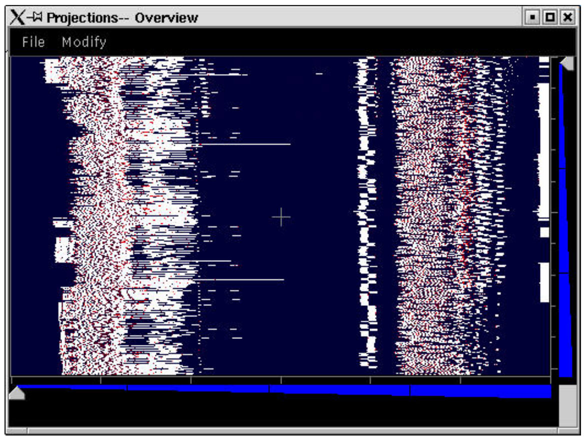

(b) Improvement by using “wrapping”(590ms)

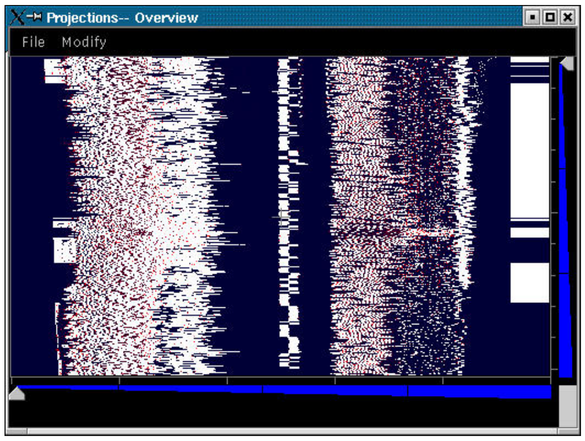

(c) Final result with load-vectors(480ms)

Figure 4.2: Solving the problem of load imbalance on 1024 processors

This was partially alleviated by using a modified version of 2.7:

$$pe(R(s,p)) = (4\mathcal{P} \times \frac{p \times n_s + s}{N \times n_s})\%\mathcal{P} \tag{4.1}$$

This scheme assumes the presence of 4 times the actual number of processors, get the processor number, and “wraps” it over the available number of processors, thus diversifying the sizes of planes present on each processor. The result of this is seen in figure 4.2, (b).

Although better than before, it is clear (by looking at a few long lines in the overview figure) that it does not achieve a good load balance, leaving a few highly overloaded processors.

We then explicitly took in to account the number of non-zeroes on each plane (alluded to in section 2.1.2). We defined a "load-vector" $\mathcal{L}$ and a "cumulative" load-vector $\mathcal{C}$ of size N and define the mapping in terms of them.

$$\mathcal{L}[i] = number\ of\ non\ zeros\ in\ plane\ i\ over\ all\ states$$

$$\mathcal{C}[i] = \sum_{j<=i} \mathcal{L}[j]$$

$$pe(G(s,p)) = \frac{\mathcal{C}[p-1] + \frac{s}{n_s} \times \mathcal{L}[p]}{l} \tag{4.2}$$

where $l = \frac{\sum_p \mathcal{L}[p]}{\mathcal{P}}$ is the desired average load per processor

The best performance was obtained when we explicitly considered the load caused by each g-space plane as in equation 4.2.

This mapping produced much better load balance, as seen in figure 4.2 However, it is clear that transforming our knowledge of the number of non-zeroes in each plane into a balanced mapping is difficult. We are therefore planning to use Charm++'s automatic load balancers, modified to allow programmers to specify partial mappings (as we need for R, as explained in Sec. 2.1.2). Our preliminary results in this directions have shown promise. E.g. on 512 processors, the automatic balancer leads to a step time of 620 ms, as opposed to 650 ms with the above manual mapping.

Chapter 5

Conclusion

We have described the parallelization of the CP method using Charm++, and our efforts to scale the benchmark to over 1500 processors, with a fixed problem size of 128 states. This is unprecedented since all earlier efforts either find scaling beyond 128 processors difficult ([?], or scale only when the problem size is proportional to the number of processors ([?]). Virtualization and adaptive overlap of communication, automatically engendered by Charm++, are clearly helpful for this application. Our results, both in absolute performance, and number of processors used, mark a significant improvement.

The floating point performance achieved is a relatively small fraction of the peak capability of the machine. The large volume of data communicated non-locally (3.5 GB on 1024 processors) is primarily responsible for this and we have identified several avenues for improvement.

The FFTs in g-space can be made more efficient by making assumptions about the nature of data-distribution in g-space. For example, if we assume that along any one axis, there are only two contiguous regions of non-zero data, the overhead when performing transposes can be significantly reduced. Also, the data in g-space is conjugate symmetric and this can be used to perform FFTs whilst "double-packing" the data. This will not only reduce the amount of computation required, but also reduce the amount of communication involved in the transposes.

The amount of communication involved in orthonormalization is very large in volume.

We intend to explore another dimension in the parallelization of the S matrix computation, which will reduce the overall amount of data sent.

Appendix Software Implementation

Charm++ and our implementation of CPAIMD using it are freely available for download at http://charm.cs.uiuc.edu. You can obtain the current code by following the links for "Research" and "Ab initio molecular dynamics".

Here is a list of the object collections used in the code and their corresponding Charm++ proxies.

- $G(s,p)$: gSpacePlaneProxy.

  This is a 2-D chare array, with the x-index being the state number and the y-index being the plane number. Note that if there is more than one plane held in a single array element, then the index is the smallest plane number among the available plane numbers. The number of planes in each object is controlled by the variable config.gSpacePPC. Only the non-zero planes are inserted, and the axis of decomposition is the x-axis.

- $A(s,p)$: particlePlaneProxy.

  This is a 2-D chare array, and is bound to the gSpacePlaneProxy, which implies that the elements particlePlaneProxy(s, p) and gSpacePlaneProxy(s, p) are always present on the same processor. This chare array is used for the particle/atom computation.

- $R(s,p)$: realSpacePlaneProxy.

  This also is a 2-D chare array, and its elements have the states in real-space. Again, if there is more than one plane held in a single array element, then the index is the smallest plane number among the available plane numbers. The axis of decomposition is the y-axis, and the number of planes in each object is controlled by the variable config.realSpacePPC.

- "ρ arrays": rhoRealProxy and rhoGProxy.

  The density in real-space is represented by a 1-D chare array, with proxy "rhoRealProxy" and the density in fourier-space is represented by another 1-D chare array, with proxy "rhoGProxy". The structure of the rhoReal array reflects that of the realSpacePlane array. The axis of decompostion is the y-axis and the number of planes per object is the same in the two arrays. The rhoG array has a different axis of decomposition and the number of planes per object is controlled by config.rhoGPPC. The array indices of both rhoReal and rhoG are continuous, i.e., even if there is more than one plane per object, the array indices progress as $0, 1, 2, \ldots$

- $S_{arr}(x, s1, s2, c)$: sCalculatorProxy

  The parameter γ is controlled by the variable config.sGrainSize. The elements that are inserted have s1 ¡= s2 and have x-coordinates corresponding to the non-zero planes.

Important groups and their uses:

- atomsGrpProxy: proxy for group used to replicate atom/particle information on all processors.

- scProxy: proxy for group used for making QC-specific constants available on all processors.

- sReducerProxy: proxy for group used for performing reductions over the S_{arr} elements.